JEM

Article

Myeloid-targeted immunotherapies act in synergy to induce inflammation and antitumor immunity

Curtis J. Perry,[1]* Andrés R. Muñoz-Rojas,[3]* Katrina M. Meeth,[2] Laura N. Kellman,[3] Robert A. Amezquita,[1,4] Durga Thakral,[2] Victor Y. Du,[1] Jake Xiao Wang,[2] William Damsky,[1,2] Alexandra L. Kuhlmann,[1] Joel W. Sher,[3] Marcus Bosenberg,[2] Kathryn Miller-Jensen,[3] and Susan M. Kaech[1]

[1]Department of Immunobiology and [2]Department of Pathology, Yale University School of Medicine, New Haven, CT
[3]Department of Biomedical Engineering, Yale University, New Haven, CT
[4]Howard Hughes Medical Institute, Chevy Chase, MD

Eliciting effective antitumor immune responses in patients who fail checkpoint inhibitor therapy is a critical challenge in cancer immunotherapy, and in such patients, tumor-associated myeloid cells and macrophages (TAMs) are promising therapeutic targets. We demonstrate in an autochthonous, poorly immunogenic mouse model of melanoma that combination therapy with an agonistic anti-CD40 mAb and CSF-1R inhibitor potently suppressed tumor growth. Microwell assays to measure multiplex protein secretion by single cells identified that untreated tumors have distinct TAM subpopulations secreting MMP9 or cosecreting CCL17/22, characteristic of an M2-like state. Combination therapy reduced the frequency of these subsets, while simultaneously inducing a separate polyfunctional inflammatory TAM subset cosecreting TNF-α, IL-6, and IL-12. Tumor suppression by this combined therapy was partially dependent on T cells, and on TNF-α and IFN-γ. Together, this study demonstrates the potential for targeting TAMs to convert a "cold" into an "inflamed" tumor microenvironment capable of eliciting protective T cell responses.

INTRODUCTION

Melanoma is a challenging disease as it readily metastasizes, and chemotherapy does not improve survival (Flaherty et al., 2013). Inhibitors of mutant B-raf (vemurafenib and dabrafenib) improve survival compared with dacarbazine chemotherapy, and survival is further prolonged with the addition of mitogen-activated protein kinase kinase (MEK) inhibitor treatment (Flaherty et al., 2012; Hauschild et al., 2012). Responses to these targeted therapies, however, typically last less than a year and are limited to the subset of melanomas with *Braf* mutations. After Food and Drug Administration approval, immune checkpoint inhibitors are now the frontline treatment for most patients with metastatic melanoma. Responses to CTLA-4 or PD-1 inhibitors are seen in up to 19 and 40% of melanoma patients, respectively (Larkin et al., 2015). The combination of the CTLA-4 and PD-1 inhibitors results in a higher response rate of 57.6%, with a median progression-free survival of 11.5 mo (Larkin et al., 2015). While these are major advances in cancer care, the current challenge is that not all patients respond, and many develop acquired resistance or must discontinue treatment as a result of adverse immune-associated toxicities. Multiple clinical trials of PD-1/PD-L1 inhibitors have shown that a lack of PD-L1 expression on tumor cells or in the tumor microenvironment (TME), including expression on myeloid cells, is associated with resistance to therapy (Larkin et al., 2015). Additionally, tumors displaying low levels of T cell infiltration, yet a relative abundance of tumor-associated macrophages (TAMs), tend to show reduced responsiveness to PD-1/PD-L1 inhibitors (Tumeh et al., 2014). Therefore, new approaches are sorely needed for patients who do not respond to anti–PD-1– or anti–CTLA-4–based regimens or who develop acquired resistance.

TAMs, tumor-associated neutrophils (TANs), and myeloid-derived suppressor cells are pivotal in influencing the nature of the TME and can serve as both positive and negative mediators of tumor growth. TAMs can mediate direct antitumor cytotoxicity and the presentation of tumor-associated antigens. However, they can also foster tumor development by secreting growth factors such as insulin-like growth factor 1 (IGF1) and platelet-derived growth factor (PDGF), promoting angiogenesis via vascular endothelial growth factor, and favoring tumor dissemination by producing matrix-degrading enzymes (Pollard, 2004). TAMs are abundant in the melanoma TME and typically comprise 5–30% of immune cells in metastatic deposits (Hussein, 2006). TAMs and myeloid-derived suppressor cells can be associated with resistance to immune checkpoint inhibitors and suppress adaptive immune responses via a variety of mechanisms, including

*C.J. Perry and A.R. Muñoz-Rojas contributed equally to this paper.

Correspondence to: Susan M. Kaech: susan.kaech@yale.edu; Kathryn Miller-Jensen: kathryn.miller-jensen@yale.edu

The Rockefeller University Press
J. Exp. Med. 2018 Vol. 215 No. 3 877–893
https://doi.org/10.1084/jem.20171435

(but not limited to) TGF-β, IL-10, ARG1, IDO, PGE2, and PD-L1 (Kryczek et al., 2006; Díaz-Valdés et al., 2011).

There is compelling rationale based on prior studies that drugs aimed to reprogram and stimulate macrophages and dendritic cells (DCs), such as inhibitors of CSF-1, leukocyte immunoglobulin-like receptor subfamily B, CD200, Tyro-Axl-Mer receptors, or, conversely, agonists of CD40 and TLRs, offer promise for tumor suppression (Bhadra et al., 2011; Ugel et al., 2015; Woo et al., 2015). CSF-1 is a critical growth and maturation factor for monocytes, macrophages, and DCs, and deletion of CSF-1 or its receptor (CSF-1R) interrupts the development and maintenance of mononuclear phagocytes, particularly in tissues (Wynn et al., 2013). Indeed, inhibition of CSF-1R via genetic deletion, small molecule inhibitors (CSF-1Ri), or antibody blockade has demonstrated interesting therapeutic effects in multiple tumor models as well as in humans in tenosynovial giant cell tumors (Cassier et al., 2012; Ries et al., 2014). Blockade of CSF-1R has reduced TAM numbers in some studies (Mitchem et al., 2013; Xu et al., 2013), but not all (Pyonteck et al., 2013), and therefore, it is generally well-accepted that CSF-1R inhibition rewires TAM functionality to promote tumoricidal functions (Pyonteck et al., 2013).

Another promising immunotherapy target on myeloid cells is agonistic αCD40 mAbs, which are potent stimulators of DCs, macrophages, and B cells, even independently of T cells (Beatty et al., 2011; Li and Ravetch, 2011). When combined with chemotherapy, αCD40 reversed the resistance of pancreatic tumors to αPD-1 and αCTLA-4 in a T cell–dependent manner (Beatty et al., 2011; Winograd et al., 2015). In the autochthonous mouse model used in this study, our group previously showed that CD40 agonist treatment slowed tumor growth independent of T cells and increased MHCI, MHCII, and CD86 expression by TAMs (Ho et al., 2014). Thus, CSF-1R inhibition and CD40 agonism have both been shown to therapeutically alter TAM populations in a sometimes T cell–independent manner.

While considerable attention has focused on the effects of combining drugs that target antitumor T cells, less has been done to examine potential synergistic effects of combining myeloid-targeted therapies (Wiehagen et al., 2017). We hypothesized that CSF-1R inhibition and CD40 agonism (CSF-1Ri+CD40) likely affect partially distinct pathways in myeloid cells and that combination of these drugs may be a more potent treatment to target "cold" tumors with poor T cell infiltration. Here we report that combination therapy with agonistic CD40 antibody and inhibition of CSF-1R signaling improved the therapeutic response of either agent alone in autochthonous mouse melanoma in agreement with a recent study using engrafted tumor models (Wiehagen et al., 2017). Importantly, combined CD40 and CSF-1Ri therapy induced a marked increase in a novel population of polyfunctional and inflammatory TAMs, and the therapeutic effect was partially dependent on T cells and production of the inflammatory cytokines IFN-γ and TNF-α. Thus, this work uncovers how two myeloid-targeted therapies synergize to generate an inflamed TME capable of eliciting protective antitumor T cell responses.

RESULTS

Autochthonous melanomas have abundant TAMs displaying heterogeneous phenotypes but low T cell infiltration

There is critical need for identifying treatment options for patients with tumors that display limited T cell infiltration and resistance to checkpoint inhibitors, such as PD-1/PD-L1 or CTLA-4 blockade. To address this problem, we focused on the genetically engineered mouse model of melanoma that allows induction of autochthonous tumors that express the *Braf*^{V600E} oncogene and lack the tumor suppressor *Pten*$^{-/-}$ (referred to as Braf/PTEN mice; Dankort et al., 2009). The melanomas that develop in this model display low CD8 T cell infiltration, an abundance of macrophages, and, in our hands, resistance to PD-1/PD-L1 or CTLA-4 blockade (Wang et al., 2017). Thus, the Braf/PTEN model is ideal for identifying more effective treatments for tumors largely resistant to current forms of checkpoint blockade.

To study the immune infiltrate in Braf/PTEN tumors, particularly the myeloid cells, we induced melanomas using topical tamoxifen and analyzed the tumors ∼8 wk later or when they reached end point (<2 cm^3). Initial characterization of the immune cells using flow cytometry showed that the predominant immune cell population in the tumor was TAMs (CD11b$^+$ Ly6G$^-$ CD3$^-$, including macrophages, monocytes, and eosinophils), in agreement with our previous study (Fig. 1 A and Fig. S1 A; Ho et al., 2014). Although the total population of T cells (CD4$^+$ and CD8$^+$) was substantial, further characterization by immunohistochemistry (IHC) demonstrated that T cells were sparse within the tumor compared with the epidermis, whereas F4/80$^{int/hi}$ TAMs were abundant within the tumor (Fig. 1, B and C).

Surface expression of Ly6C and F4/80 identified three distinct TAM subpopulations: cells that express high amounts of F4/80 (F4/80^{hi}) and two populations that express intermediate amounts of F4/80 with or without Ly6C (Ly6C$^+$ F4/80^{int} and Ly6C$^-$ F4/80^{int}, respectively; Fig. 1 D and Fig. S1 B). The F4/80^{hi} cells expressed the highest amounts of CCR2, CD206, and CD86 with much lower amounts of TNF-α and Ki67 (Fig. 1 E). Cells in this subset were also modestly larger than the others based on forward scatter (Fig. S1 C). PD-L1 was most highly expressed by F4/80^{hi} and Ly6C$^-$ F4/80^{int} cells, suggesting that these subpopulations contain mostly antiinflammatory TAMs. TNF-α–producing cells were enriched in the F4/80^{int} TAMs (both Ly6C$^+$ and Ly6C$^-$), and increased Ki67 expression in the Ly6C$^+$ F4/80^{int} TAMs suggested that this subpopulation was enriched for proliferating cells (Fig. 1 E and Fig. S1 B). Furthermore, CSF-1R was widely expressed by TAMs, indicating that most TAMs could be potential targets for CSF-1R inhibition (Fig. S1 B). Together, these data demonstrate phenotypic and functional diversity of TAMs within the TME.

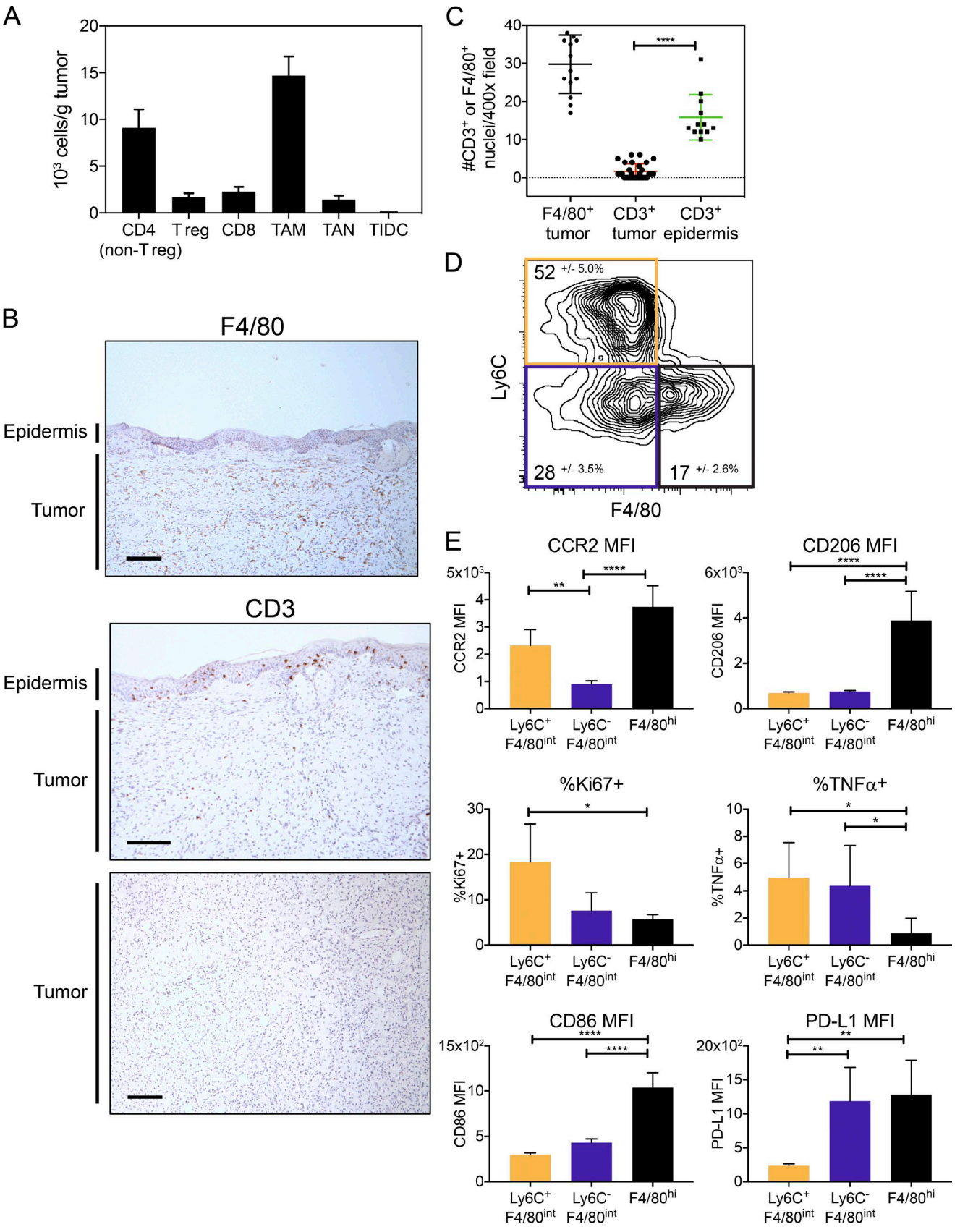

To more deeply investigate the functional heterogeneity of TAMs, we used a microwell assay for single-cell secretion profiling (Lu et al., 2013) to measure the multiplexed secretion of 15 cytokines, chemokines, and other mediators produced by single TAMs directly ex vivo (without further stimulation) isolated from 8-wk-old tumors. The panel of 15 secreted targets was designed to distinguish what is commonly referred to as M1-like and M2-like TAMs in the tumor. We sorted total TAMs as well as subpopulations based on expression of Ly6C and F4/80 (Fig. 1 D) to map secretory functions to the surface-marker subpopulations. We found that the majority of TAMs were functionally silent for the measured proteins, consistent with a quiescent state, but ∼30% of TAMs showed robust secretion of one or more proteins (Fig. 2 A). The proteins most frequently secreted by the total TAM population were MMP9 and Chi3l3, which are commonly associated with M2-like functions in macrophages (Fig. 2 B). Interestingly, the frequency of MMP9-secreting cells was significantly decreased in the Ly6C$^+$ F4/80^{int} subpopulation and increased in the Ly6C$^-$F4/80^{int} subpopulation, whereas Chi3l3 secretion showed opposite trends, suggesting that these subpopulations have distinguishing functional features (Fig. 2 C).

To identify subpopulations present within TAMs based only on single-cell secretion profiles, we combined all sorted subpopulations across three independent experiments (Fig. S2) and clustered the cells secreting at least one protein using PhenoGraph, a previously described clustering algorithm (Levine et al., 2015). We then projected the high-dimensional secretion data onto two dimensions using t-distributed stochastic neighbor embedding (t-SNE; Amir et al., 2013) to visualize functional clusters of cells in the TME (Fig. 2 D and Fig. S2). Four functional clusters were identified from the combined TAMs that could be defined based on their most predominantly secreted product(s) and that were robustly present across all biological replicates—MMP9$^+$, Chi3l3$^+$, MMP9$^+$Chi3l3$^+$, and CCL17$^+$CCL22$^+$ clusters—so we focused our analysis on these clusters (Fig. 2 E and Fig. S2). The remaining cells occupied functionally variable clusters that likely reflect intertumoral heterogeneity. These data demonstrate, at single-cell resolution, the functional diversity within TAMs in melanomas.

Comparing the functional clusters to subpopulations based on surface marker expression, we found that the Ly6C$^+$ F4/80^{int} subpopulation was dominated by cells from the Chi3l3$^+$ cluster and largely excluded cells from the other functional clusters (MMP9$^+$, MMP9$^+$/Chi3l3$^+$, and CCL17$^+$/CCL22$^+$; Fig. 2 F). Chi3l3$^+$/MMP9$^+$ cells were predominantly found in the F4/80^{hi} subpopulation, whereas MMP9$^+$-only cells were predominantly found in the Ly6C$^-$F4/80^{int} subpopulation. Altogether, these data show that TAMs within late-stage tumors secrete mediators that are commonly associated with M2-like immune responses, but they comprise functionally distinct subsets of cells even within this M2-like category. Although functional clusters may reflect some temporal differences in TAM secretion, the observation that subpopulations defined by surface marker expression enrich for or exclude the most commonly observed functional clusters suggests that these clusters are not wholly unstable. However, clearly a large amount of functional diversity remains within each subpopulation and further characterization will be needed to better link phenotype to function.

Combination therapy with agonistic CD40 and CSF-1R inhibition constrains tumor growth more effectively than monotherapy

We sought to better understand how TAM function was affected by myeloid-targeted treatments of clinical interest, specifically CD40 agonistic antibody (CD40) and a selective small molecule inhibitor of CSF-1R (CSF-1Ri; Beatty et al., 2011; Ryder et al., 2013; Ho et al., 2014). To this end, tumor-bearing mice were treated with CSF-1Ri chow (600 mg PLX6134/kg chow) and/or CD40 agonistic antibody (10 mg FGK4.5 clone /kg every 3 d i.p.) starting at day 30 after tumor induction, when tumors were measurable but total volume was <100 mm^3. CD40 treatment significantly slowed tumor growth (CD40 vs. control, $P = 0.02$; Fig. 3 A), consistent with our previous study (Ho et al., 2014). CSF-1Ri was also found to inhibit Braf/PTEN tumor progression (CSF-1Ri vs. control, $P = 0.02$; Fig. 3 A). Combined treatment yielded improved control of tumor growth compared with either treatment alone (CSF-1Ri+CD40 vs. CD40, $P = 0.04$; CSF-1Ri+CD40 vs. CSF-1Ri, $P = 0.04$), and the combination CSF-1Ri and CD40 treatment was dramatically more effective than controls (CSF-1Ri+CD40 vs. control, $P < 0.0001$). Both CD40 and CSF-1Ri roughly halved tumor volume 30 d after initiating treatment, whereas

Figure 1. **Myeloid cell heterogeneity in Braf/Pten tumors. (A)** Immune cellularity of tumors from flow cytometry at end point, 8 wk after tumor induction. TAMs were defined as CD45$^+$ CD11b$^+$ Ly6G$^-$, distinct from TANs (CD45$^+$ CD11b$^+$ Ly6G$^+$), and tumor-infiltrating DCs (TIDCs; CD45$^+$ CD11c$^+$ CD11b$^-$ Ly6G$^-$). Regulatory CD4$^+$ T (T reg) cells were defined as CD45$^+$ CD3$^+$ CD4$^+$ Foxp3$^+$ and distinguished from non-regulatory CD4$^+$ T cells by Foxp3 expression. CD45$^+$ CD8$^+$ CD3$^+$ defined CD8 T cells. Data are from three independent experiments (n = 9–12). **(B)** F4/80 and CD3 IHC representative images from tumors at end point (1 cm^3). Bars, 150 µm. **(C)** F4/80$^+$ and CD3$^+$ nuclei were counted per hpf from IHC images of tumors (as in B) from two independent experiments, 6–15 hpf/tumor (n = 12–30). Significance was determined by unpaired Student's t test. **(D)** Contour plot shows expression of Ly6C and F4/80 on TAMs from end point (1 cm^3) tumors. Plot isconcatenated (combined) from each individual mouse tumor (n = 6). The mean ± SD for each subset (Ly6C$^+$ F4/80^{int}, Ly6C$^-$ F4/80^{int}, and Ly6C$^-$ F4/80^{hi}) is reported. Data are from one experiment and are representative of three experiments (n = 6 each group). **(E)** Bar graphs show mean fluorescence intensity (MFI) or percentage expressing the indicated proteins for the three TAM subsets outlined in D from end point (1 cm^3) tumors. Data are from one experiment and are representative of three experiments (n = 6 each group). Significant differences between groups were determined by one-way ANOVA with Holm-Sidak multiple comparisons correction; *, $P < 0.05$; **, $P < 0.01$; ****, $P < 0.001$.

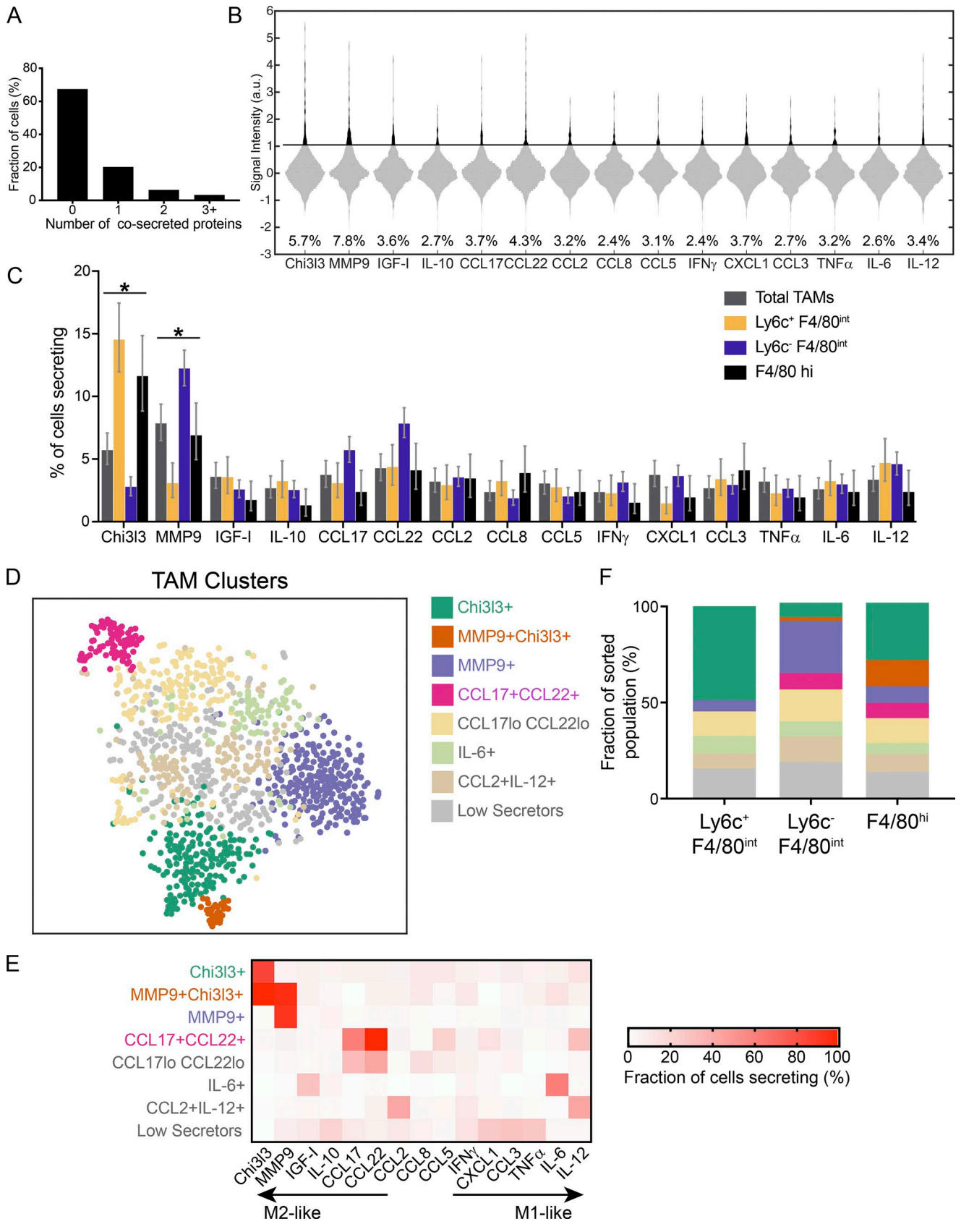

CSF-1Ri+CD40-treated tumors were only 13% the size of controls (control mean, 675 mm^3; CD40 mean, 369 mm^3; CSF-1Ri mean, 360 mm^3; and CSF-1Ri+CD40 mean, 87 mm^3). Altogether, combined treatment with CD40 and CSF-1Ri more effectively suppressed tumor growth than either CD40 or CSF-1Ri alone.

To understand how targeting myeloid cells with CD40 and CSF-1Ri mediated tumor suppression, we characterized the density and phenotypes of infiltrating immune cells at the end point (day 60) for treated and untreated tumors. Although we did not observe differences in the density of tumor associated T cells (including T regulatory cells) or DCs ($CD11c^+$ $CD11b^-$), CSF-1Ri+CD40 treatment caused a marked increase in density of TAMs ($P < 0.0001$; Fig. 3 B) and density and proportion of TANs ($CD11b^+$ $Ly6G^+$ $CD3^-$; $P < 0.001$; Fig. 3 B and Fig. S3). When we analyzed the TAM populations, we observed differences in phenotype and function. Phenotypically, CSF-1Ri+CD40 increased $Ly6C^+$ $F4/80^{int}$ TAM density considerably ($P = 0.008$; Fig. 3 C). Furthermore, combined treatment with CD40 and CSF-1Ri caused a reduction in the $F4/80^{hi}$ $CD206^+$ $PD\text{-}L1^+$ TAM population more than CSF-1Ri alone (control vs. CSF-1Ri+CD40, $P = 0.008$; Fig. 3 D). Functionally, CSF-1Ri+CD40 treatment increased TNF-α production, particularly in the $Ly6C^+$ $F4/80^{int}$ TAMs, compared with control tumors ($P = 0.0001$; Fig. 3 E). In agreement with a previous study, CSF-1Ri increased TAN infiltration, an effect that was substantially enhanced by CSF-1Ri+CD40 combination treatment ($P < 0.001$; Fig. 3, B and F; Ngiow et al., 2016). Collectively, these results demonstrate that the suppression of tumor growth by combination CSF-1Ri+CD40 treatment correlates tightly with increased infiltration of neutrophils and macrophages, particularly $Ly6C^+$ $F4/80^{int}$ TAMs and production of TNF-α.

Combination CD40 and CSF-1Ri drives a TAM inflammatory transcriptional program

To begin to understand how these treatments modulated TAMs to control tumor growth and to possibly illuminate additional biomarkers of response, we examined the transcriptomes of $CD11b^+$ $Ly6G^-$ cells treated with CD40 or CSF-1Ri, alone or in combination, relative to control, using high-throughput RNA-sequencing. Principal component analysis on the genome-wide dataset demonstrated that treating with CD40 and CSF-1Ri individually caused largely nonoverlapping changes in transcription, as indicated by their movement along orthogonal principal components relative to the control (Fig. 4 A). Importantly, combination therapy was visualized as a systems-level combination of each individual treatment in principal component space.

We then examined the mRNAs most altered by either treatment alone or in combination relative to controls (log_2fold change > 1.5; $P < 0.01$) by unsupervised hierarchical clustering (Fig. 4 B). Five major gene patterns emerged from the clustering of genes. Cluster 1 comprises genes that were up-regulated by CD40 and CSF-1Ri+CD40 treatment but are mostly unaffected by CSF-1Ri, suggesting that CD40 is the primary driver of this cluster in the combination treatment. Notable genes in this cluster include *Tnfa*, *Ifng*, *Il12b*, and *Cxcl9*; interestingly, for *Tnfa* and *Il12b*, CSF-1Ri+CD40 appears to have a synergistic effect on expression. In contrast to Cluster 1, Cluster 5 contains genes substantially down-regulated by CSF-1Ri and CSF-1Ri+CD40 treatments, but are largely unaffected by CD40, suggesting that CSF-1Ri is the driver of this cluster in the combination treatment. Cluster 5 genes include *Cd36* and *Fabp4*, suggesting alterations in lipid homeostasis in the TAMs after treatment. Cluster 2 includes genes that are modestly up-regulated by CD40 and CSF-1Ri individually, leading to a stronger up-regulation when combined. Finally, Clusters 3 and 4 include, for the most part, genes that are differentially affected by CD40 versus CSF-1Ri and for which the combination treatment yields an intermediate response. In summary, these data show that CSF-1Ri and CD40 agonism elicit predominantly distinct changes in gene expression in the $CD11b^+$ cells, indicating they target different biological processes in myeloid cells. The net result of the changes in myeloid gene expression from the combination of CSF-1Ri+CD40 treatment reveal additive effects by the individual treatments, but also synergy in the expression of several proinflammatory genes (e.g., *Tnfa*, *Ifng*, *Il6*, and *Il12b*).

We further examined our dataset with Gene Set Enrichment Analysis. Although CSF-1Ri and CD40 treatments did not closely match any immunological signatures in the immunological database of Molecular Signals Database, com-

Figure 2. **Functional heterogeneity in TAM subsets in Braf/Pten melanomas. (A)** Polyfunctionality of TAMs isolated from end point (1 cm^3) tumors. Bar graphs show fraction of single cells captured cosecreting 0, 1, 2, or >3 targets. Data are pooled from two independent experiments. **(B)** Violin plots of single-cell secretion profiling results for sorted $CD11b^+$ TAMs. Black bar indicates calculated threshold of detection. Data are pooled from two independent experiments. a.u., arbitrary units. **(C)** Fractions of cells secreting each target from sorted subpopulations. Error bars represent the 95% confidence interval calculated by bootstrapping (see Statistics in Materials and methods for details). Statistical significance determined by nonoverlapping confidence intervals. *, $P < 0.05$. **(D)** 2D t-SNE representation of single TAMs based on the secretion levels of 15 proteins. Functional TAM clusters were identified with PhenoGraph from three independent tumors (Fig. S2). TAMs were isolated from end point (1 cm^3) tumors, sorted into subpopulations by surface markers ($Ly6C^+$ $F4/80^{int}$, $Ly6C^-$ $F4/80^{int}$, and $Ly6C^-$ $F4/80^{hi}$), and analyzed for secretion. TAMs that did not express any of the 15 measured targets above the detection limit were excluded from the analysis. t-SNE map shows all sorted TAM subpopulations pooled together from two independent experiments. Clusters coded by color (see key). **(E)** Percentage of cells in each cluster from D secreting each of the 15 measured targets. Cluster names are based on the primary secreted target(s) in each cluster. **(F)** Stacked bar graph shows the distribution of functional clusters in D within each sorted subpopulation ($Ly6C^+$ $F4/80^{int}$, $Ly6C^-$ $F4/80^{int}$, and $Ly6C^-$ $F4/80^{hi}$). Clusters coded by color (see key).

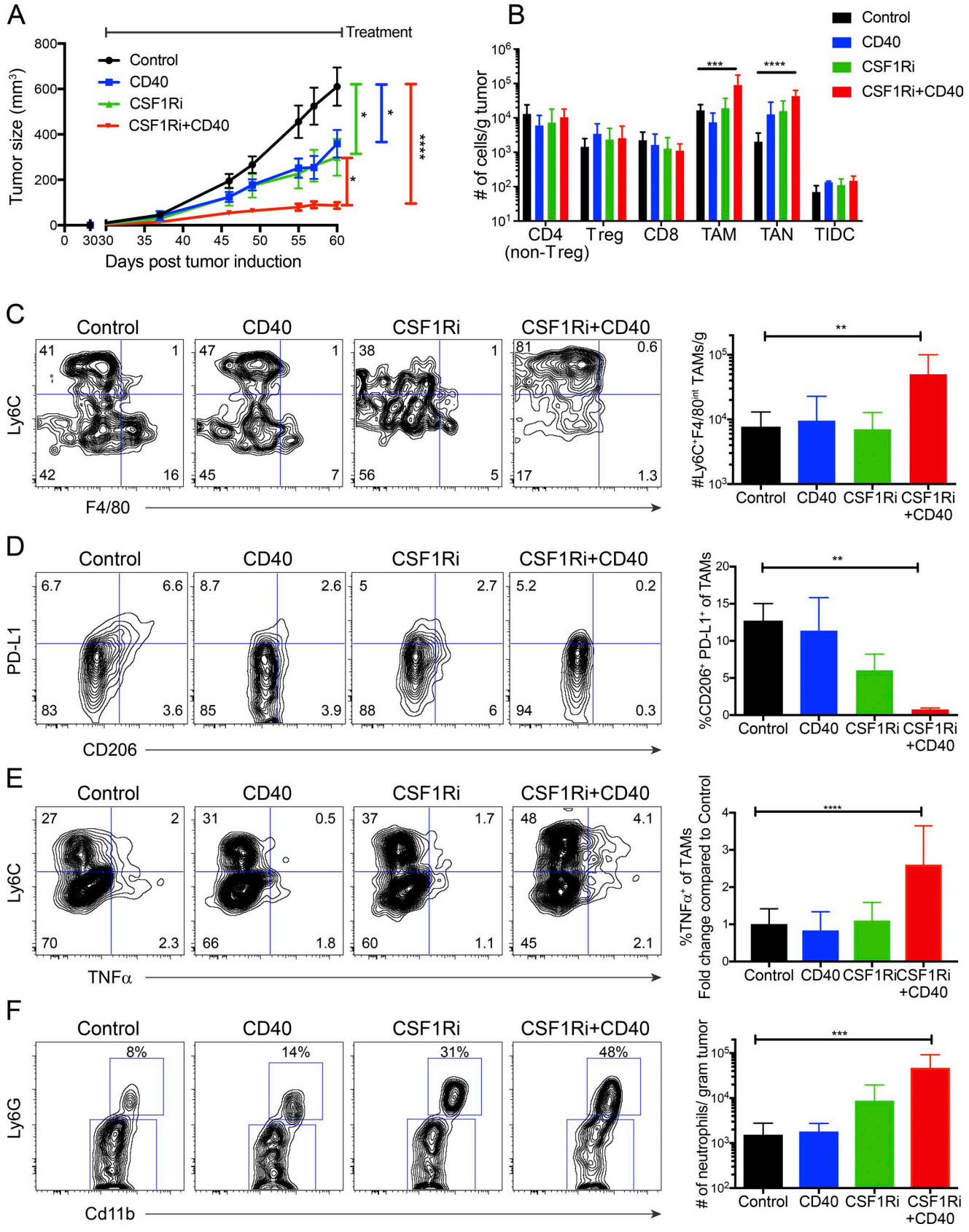

bined CSF-1Ri+CD40 had a strikingly similar signature to myeloid cells exposed to a variety of inflammatory stimulants, most closely reflected by murine bone marrow–derived macrophages treated with LPS (Fig. 4 C). This motivated us to look specifically at categories of NF-κB target genes that are significantly affected by LPS treatment, including transcription factors, cytokines, and chemokines (Fig. 4 D). Indeed, most of these NF-κB target genes associated with inflammation were strongly up-regulated by CSF-1Ri+CD40 treatment. Finally, Ingenuity Pathway Analysis identified TNFR1 and TNFR2 signaling and acute phase response signaling among the top genetic signatures produced by the CSF-1Ri+CD40 treatment combination (Fig. S4 A), matching what we observed with Gene Set Enrichment Analysis. Thus, gene expression analysis not only revealed several biomarkers of response that may be relevant for assessing therapeutic activity in ongoing clinical trials using these drugs, but illuminated lead biological factors that may cause tumor regression (as examined in the following paragraphs).

Combined CSF-1Ri and CD40 agonist treatment drives an inflammatory response by a subset of polyfunctional TAMs

To better understand functional correlates of response in myeloid-targeted immunotherapies, we performed multiplexed single-cell secretion profiling on TAMs isolated from control and CSF-1Ri+CD40-treated tumors. CSF-1Ri+CD40 treatment significantly increased the fraction of TAMs secreting inflammatory cytokines and chemokines, including TNF-α, IL-6, IL-12, CCL3, CXCL1, and IFN-γ (Fig. 5 A and Fig. S4 B, $P < 0.05$ by bootstrapping), in agreement with the RNA sequencing results (Fig. 4). Interestingly, CSF-1Ri+CD40 treatment also significantly increased the fraction of cells secreting Chi3l3 fivefold but reduced the fraction of cells secreting MMP9 by more than 60% (Fig. 5 A and Fig. S4 B). In general, the change in mRNA target expression in TAMs and the change in fraction of TAMs secreting each target were correlated in response to CSF-1Ri+CD40 treatment (Fig. 5 B). Overall, therapeutic response to CSF-1Ri+CD40 treatment was associated with the loss of M2-like MMP9 secretion and the gain of M1-like inflammatory secretion functions within the TAM population.

We again used PhenoGraph to identify functional clusters from the single-cell secretion profiles of TAMs secreting at least one protein and then mapped cells in two-dimensional (2D) t-SNE space to see how CSF-1Ri+CD40 treatment altered the functional clusters identified in control tumors. PhenoGraph analysis showed that a new polyfunctional cluster emerged after CSF-1Ri+CD40 treatment (light blue cluster, Fig. 5 C). This cluster was defined by cosecretion of Chi3l3 and the inflammatory cytokines TNF-α, IL-6, and IL-12, as well as other factors (Fig. 5, D and G), and it was almost completely absent from control tumors (Fig. 5 E). To confirm the presence of polyfunctional inflammatory TAMs, we calculated the fraction of active cells (i.e., secreting at least one target) that were cosecreting TNF-α, IL-6, and IL-12, and found that this subset of TAMs was significantly larger in treated tumors (Fig. 5 F). CSF-1Ri+CD40 treatment also increased the size of the Chi3l3$^+$ cluster (Fig. 5 E), indicating that the overall increase in Chi3l3 secretion included both polyfunctional TAMs and an increase in TAMs that only secrete Chi3l3. Notably, the substantial decrease in MMP9 caused by the CSF-1Ri+CD40 treatment was mostly because of the loss of cells that solely produced MMP9 (purple cluster, Fig. 5, C and E). The less frequent Chi3l3$^+$ MMP9$^+$ cluster (orange cluster) remained in similar proportion after CSF-1Ri+CD40 treatment (Fig. 5 E), indicating a selective depletion of MMP9$^+$-only secreting cells (purple cluster). The relative contribution of the CCL17$^+$CCL22$^+$ cluster also decreased after CSF-1Ri+CD40 treatment (pink cluster, Fig. 5, C and E). Collectively, these data demonstrate that CSF-1Ri+CD40 treatment selectively reduces specific functional clusters of cells, while adding functionality to others. In particular, a substantial fraction of CSF-1Ri+CD40-treated TAMs acquired a robust polyfunctional inflammatory phenotype while simultaneously depleting MMP9$^+$ cells.

Combination treatment efficacy is T cell dependent and increases IFN-γ expression by T cells

While TAMs displayed profound functional changes in response to combination therapy, we sought to understand whether other cell types were involved in treatment efficacy. To this end, we depleted neutrophils and T cells from the mice

Figure 3. **Effects of CSF-1Ri and CD40 agonist treatment alone or in combination on TAM subsets. (A)** Braf/Pten mice were treated with CSF-1Ri (600 mg PLX6134/kg chow) and/or CD40 (10 mg FGK4.5/kg every 3 d) 30 d after tumor induction until end point (day 60) for a total of 10 doses of FGK4.5. Line graphs show size of Braf/Pten melanomas over time. Data are the mean ± SEM of tumor size of five independent experiments (n = 15–25). Significance was determined by one-way ANOVA with Holm-Sidak correction for multiple comparisons and post-hoc unpaired Student's t tests at the end point (day 60). **(B)** Bar graphs show numbers per gram of tumor of infiltrating immune cell types (as indicated) in control tumors or tumors treated with CSF-1Ri, CD40, or the combination as measured by flow cytometry at the end point (day 60). Immune cell populations defined as in Fig. 1 A. Data are from two independent experiments (n = 6–12). Significance was determined using one-way ANOVA with Holm-Sidak multiple comparisons correction. **(C–E)** Flow plots show number of Ly6C$^+$ F4/80^{int} TAMs (C), percentage of CD206+PD-L1+ TAMs (D), and percentage of TAMs expressing TNF-α (E) from control tumors or those treated with CSF-1Ri, CD40, or the combination at the end point (day 60). Flow plots show concatenated plots of each individual mouse tumor. Data are from one experiment (n = 3–6) representative of five independent experiments (total n = 8–17). Significance was determined by one-way ANOVA with Holm-Sidak multiple comparisons correction. **(F)** Flow plots show infiltrating TANs in the tumors as determined by Ly6G$^+$ CD11b$^+$ staining and flow cytometry. Data are from three independent experiments (n = 6–11). Significance determined by one-way ANOVA with Holm-Sidak multiple comparisons correction; *, $P < 0.05$; **, $P < 0.01$; ***, $P < 0.005$; ****, $P < 0.001$.

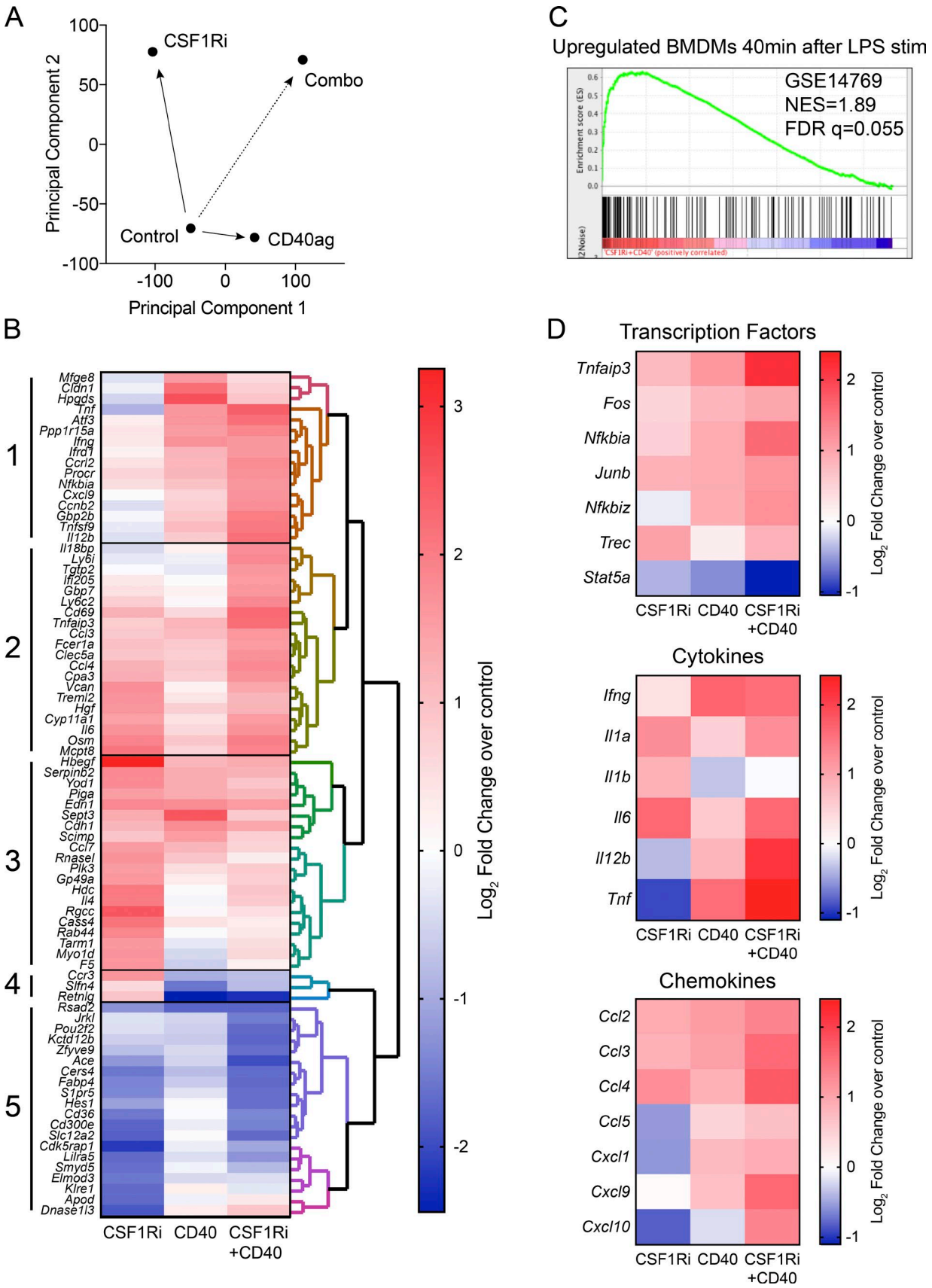

and compared tumor growth after CSF-1Ri+CD40 treatment. Depletion of TANs had no noticeable effect on treatment efficacy (Fig. S5 A), suggesting that CSF-1Ri+CD40 treatment works independently of neutrophils despite the large influx of these cells after treatment. Interestingly, although either CD40 agonist or CSF-1Ri monotherapies suppressed Braf/Pten tumor growth independently of T cells (Ho et al., 2014) and (Fig. S5 B), depletion of CD4 and CD8 T cells markedly decreased the effectiveness of CSF-1Ri+CD40 treatment ($P < 0.001$; Figs. 6 A and Fig. S5 C). This suggests that CSF-1Ri+CD40 treatment converts an ineffective antitumor T cell response to one that is effective.

To further understand the role of T cells in the antitumor response after CSF-1Ri+CD40 treatment, we analyzed the transcriptomes of T cells ($CD45^+$ $CD3^+$) using high-throughput RNA sequencing. Ingenuity Pathway Analysis indicated that chemokine signaling and interferon signaling where were the top two modulated pathways by CSF-1Ri+CD40 treatment (Fig. 6 B), with a more than twofold increase in transcription of IFN-γ ($P < 0.01$) with CSF-1Ri+CD40 treatment (Fig. 6 C). However, we observed persistently low expression of TNF-α by T cells both by RNA and flow cytometry (Fig. S5 D and data not depicted). Thus, CSF-1Ri+CD40 combination therapy induces greater amounts of IFN-γ expression in T cells, which is often a necessary component of protective antitumor immunity.

TNF-α and IFN-γ contribute to tumor growth suppression by combined CSF-1Ri+CD40 agonist therapy

Given that CSF-1Ri+CD40 treatment increased the proinflammatory secretion displayed by TAMs (Fig. 5), revealed a strong TNF-α gene expression signature in TAMs (Fig. 4 C), and increased IFN-γ gene expression by T cells (Fig. 6, B and C), we hypothesized that TNF-α and IFN-γ may be required for the therapeutic effects of CSF-1Ri+CD40-mediated suppression of melanoma growth. To test these ideas, we coadministered CSF-1Ri+CD40 treatment along with blocking antibodies to TNF-α and IFN-γ (either alone or in combination; Ho et al., 2014; Maltby et al., 2014). Blocking either TNF-α alone (gray line) or IFN-γ alone (green line) modestly reduced the therapeutic efficacy of CSF-1Ri+CD40 treatment (Fig. 6 D; and Table 1). However, blocking both TNF-α and IFN-γ simultaneously (blue line) reduced the therapeutic benefit of CSF-1Ri+CD40 by more than 50% compared with control tumors ($P = 0.02$; Fig. 6 D; and Table 1). These data support the conclusion that TNF-α and IFN-γ, which are preferentially produced by TAMs and T cells, respectively, are important underlying factors by which CSF-1Ri+CD40 combination therapy suppresses tumor growth and provides greater insight into the rational combination of innate- and adaptive-targeted immunotherapy.

DISCUSSION

More clarity is needed on how macrophages, DCs, and other innate immune cell types regulate the "immunologic tone" of the TME and antitumor T cell responses. Particularly, there is a need to elucidate the underlying mechanisms of myeloid-targeted immunotherapies to determine the context by which they boost antitumor immunity and whether they can synergize when combined. Also, it is important to investigate whether stimulation of the innate immune cells can convert an uninflamed tumor landscape to an inflamed one that enhances responsiveness to checkpoint blockade (like inhibitors of PD-1/PD-L1 signaling). Therefore, we explored the mechanisms by which the combination of anti-CD40 mAbs and CSF-1R inhibitors improved the therapeutic response of either agent alone in an autochthonous, poorly immunogenic mouse model of melanoma. As part of this study, we present the first single-cell functional secretion analysis of TAMs isolated directly from an endogenous melanoma model. By combining analysis of subpopulations defined by surface markers, RNA sequencing of total TAMs, and single-cell secretion profiling of individual TAMs before and after treatment, we obtained a new understanding of how CSF-1Ri+CD40 combine to inhibit tumor growth. Namely, combination treatment induced a polyfunctional TAM subset secreting multiple inflammatory cytokines (including TNF-α, IL-6, and IL-12) concomitant with a loss of $MMP9^+$ TAMs and an effective IFN-γ^+ T cell response in previously uninflamed tumors. Moreover, we found that TNF-α and IFN-γ were required for the antitumor effects of the combined treatment, pointing to a model that this drug combination creates robust antitumor immune responses via the joint stimulation of TNF-α–producing TAMs and IFN-γ–producing T cells.

This study identified therapeutic synergy between two myeloid-targeting therapies in an autochthonous, poorly immunogenic model and is similar in several ways to another recent study (Wiehagen et al., 2017) and the companion study

Figure 4. **Changes in myeloid cell mRNA expression patterns in response to CSF-1Ri and CD40 agonist treatment alone or in combination. (A)** Principal component analysis of RNA sequencing data: all expressed genes were analyzed by principal component analysis (SIMCA). Data are from three independent experiments of $CD11b^+$ TAMs sorted from end point (day 60)-pooled tumors treated as described in Fig. 3 A and Fig. S1 A with mRNA isolated and libraries prepared from all four groups in triplicate ($n = 3$ for each group). **(B)** RNA sequencing profile of TAMs showing the $\log_2$fold change of treatments over control. Data are from three independent experiments ($n = 3$ each group, with three individual tumors pooled for each sample). To find differentially regulated sets of genes for signature generation, a 1.5 $\log_2$fold change difference between samples and p-value–adjusted (Holm-Sidak) to ≤ 0.01 was used. **(C)** The most enriched gene set of CSF-1Ri+CD40 is positively correlated with BMDM 40 min after treatment with LPS (GSE14769). NES = 1.89, Nominal p-value = 0.0, FDR q-value = 0.055, Family-wise error rate (FWER) p-value = 0.055. FDR, false discovery rate; NES, normalized enrichment score. **(D)** Selected transcription factors, cytokines, and chemokines consistent with inflammatory signaling by TAMs. RNA sequencing profile of TAMs showing the $\log_2$fold change of treatments over control. Data are from three independent experiments ($n = 3$ each group, with three individual tumors pooled for each sample).

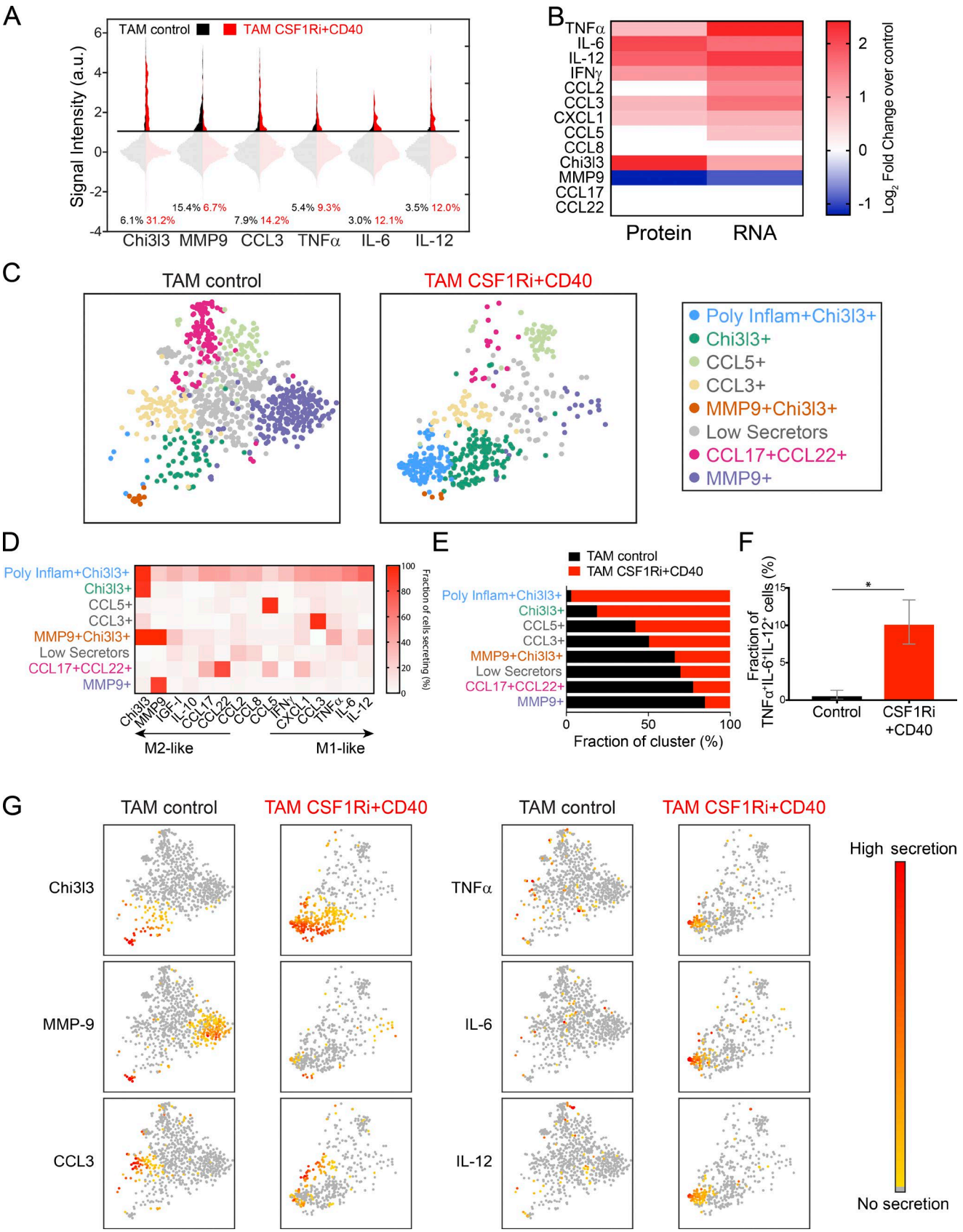

by Hoves et al., using engrafted tumor cell lines. While these three studies each use a different reagent to block CSF-1R$^+$ cells, they collectively report that when combined with agonistic CD40 mAb, there was increased infiltration of TNF-α$^+$ NOS2$^+$ Ly6C^{hi} inflammatory monocytes and Ly6G$^+$ granulocytic cells and decreased infiltration of CD206$^+$ TAMs (Youn et al., 2008; Tamoutounour et al., 2013). Moreover, this myeloid-targeted drug combination elicited IFN-γ$^+$ T cells and a protective antitumor T cell response in all the various tumor models tested (Wiehagen et al., 2017), which was unexpected in our model because each monotherapy suppressed tumor growth independently of T cells (Fig. S5 B; Ho et al., 2014). Together, these findings indicate that CSF-1Ri+CD40 combination therapy converts a "cold" tumor into an "inflamed" TME capable of eliciting protective T cell responses. Perhaps, this treatment may sensitize resistant tumors to checkpoint blockade (e.g., anti–PD-1), a direction we are currently pursuing.

At a population level, we observed a striking increase in the expression of NF-κB target genes in TAMs. CD40 is known to activate NF-κB signaling by releasing Pi3K-γ inhibition, which allows NF-κB to recruit histone acetyl transferases to modify the chromatin environment and increase gene expression (Kaneda et al., 2016). This suggests that CD40 stimulation could cause epigenetic modifications that increase coexpression of several M1- and M2-related genes simultaneously (Piccolo et al., 2017). Thus, gene expression analysis not only revealed several biomarkers of response that may be relevant for assessing therapeutic activity in ongoing clinical trials using these drugs, but also revealed lead biological factors (e.g., IFN-γ and TNF-α) that may cause tumor regression. However, our population-level mRNA analysis is fundamentally limited in resolving the function of individual cell types and how these functions contribute to tumor growth suppression.

Using single-cell multiplexed secretion profiling, we were able to observe changes in secretion functions that appeared to occur within distinct TAM subsets. Specifically, we observed that CSF-1Ri+CD40 treatment greatly augmented the infiltration of Chi3l3$^+$ and polyfunctional TNF-α$^+$, IL-6$^+$, IL-12$^+$, and Chi3l3$^+$ TAMs and decreased that of MMP9$^+$ TAMs. Chi3l3 is thought to act as a lectin and a chemoattractant for eosinophils and is commonly used as a marker for M2 activity, although its exact role in inflammation remains unclear (Zhao et al., 2013). The observed association of Chi3l3 with tumor suppression in our study begs for future investigation and correlative studies in human tumors treated with such drugs. In contrast to Chi3l3, MMP9 was rarely, if ever, observed to be cosecreted with proinflammatory factors by TAMs, and instead, MMP9$^+$ cells appeared to be selectively depleted in response to combination therapy. MMP9 is a matrix metalloproteinase responsible for extracellular matrix degradation and tissue remodeling, and in the context of cancer, MMP9's remodeling activity has been associated with angiogenesis, tumor growth, invasion, and metastasis (Joyce and Pollard, 2009; Qian and Pollard, 2010; Deryugina et al., 2014). Given MMP9's known protumor role in the TME, it is possible that the decrease in MMP9-secreting cells contributes directly to inhibition of tumor growth, motivating follow-up studies on its potential as a therapeutic target. Of note, MMP9 depletion was specifically targeted to cells secreting only MMP9$^+$, and not to cells cosecreting MMP9$^+$Chi3l3$^+$, which appeared to be largely unaffected by the combination therapy.

While our work highlights the functional heterogeneity of TAMs at a single-cell level, it is unclear to what extent these clusters reflect stable functional states, or rather, reveal the inherent plasticity within the myeloid cell populations. Although myeloid cell plasticity is likely a major factor, our finding that subpopulations defined by surface marker expression enrich for or exclude the most commonly observed functional secretion clusters suggests that these clusters are not completely unstable. However, it is difficult to parse this with static measurements; dynamic measurements over time would be required to fully resolve functional plasticity. Lastly, another limitation in our single-cell analysis was that we only linked a few surface markers with effector functions. Moving forward, it will be important to better parse apart the cellular and functional phenotypes in greater detail.

Finally, we demonstrated that the effect of the combination therapy was dependent on TNF-α and IFN-γ. TNF-α is a well-characterized proinflammatory protein that induces NF-kB activation, which agrees with the observed induction of NF-κB–associated genes after combination therapy. IFN-γ, in addition to impairing tumor vascularization, is known to relax the chromatin environment in macrophages to "prime" a

Figure 5. **Combined CSF-1Ri and CD40 agonist treatment drives formation of a poly-functional inflammatory subset of TAMs. (A)** Violin plot of single-cell secretion profiling results for control and CSF-1Ri+CD40-treated TAMs. TAMs were sorted at end point (day 60) and analyzed for single-cell secretion from mice treated as described in Fig. 3 A. a.u., arbitrary units. **(B)** Heat maps of the $\log_2$fold change of CSF-1Ri+CD40 treatment over control for the percentage of TAMs secreting as measured by single-cell secretion profiling (left) and gene expression as measured by RNA sequencing (right) for the indicated targets. Nonsignificant changes ($P > 0.05$) were set to 0. **(C)** 2D t-SNE representation of single TAMs from control and CSF-1Ri+CD40-treated tumors based on secretion levels of 15 proteins. Functional TAM subsets were identified by clustering with PhenoGraph. TAMs that did not express any of the 15 measured targets above the detection limit were excluded from the analysis (∼50% in control and ∼50% in treated; data not depicted). **(D)** Percentage of cells in each subset in C secreting each target signal. Cluster names are based on the primary secreted target(s) in each cluster. **(E)** Functional TAM subsets ranked by their prevalence in CSF-1Ri+CD40 treatments versus controls, normalized by cell number. **(F)** Fraction of cells cosecreting TNF-α, IL-6, and IL-12 in control and CSF-1Ri+CD40-treated tumors. Error bars represent a 95% confidence interval calculated by bootstrapping. Statistical significance determined by nonoverlapping confidence intervals; *, $P < 0.05$. **(G)** 2D t-SNE representation of single-cell cytokine expression from individual TAMs from control and CSF-1Ri+CD40-treated tumors as in C colored by relative expression of the indicated cytokine.

Table 1. **Log-rank p-values for survival curves (Mantel-Cox)**

Two-way comparison			Log-rank p-value
Control	vs.	CSF-1Ri+CD40	0.0011
Control	vs.	CSF-1Ri+CD40+αTNF-α/IFN-γ	0.0068
Control	vs.	CSF-1Ri+CD40+αTNF-α	0.0285
Control	vs.	CSF-1Ri+CD40+αIFN-γ	0.0189
CSF-1Ri+CD40	vs.	CSF-1Ri+CD40+αTNF-α/IFN-γ	0.0177
CSF-1Ri+CD40+αTNF-α	vs.	CSF-1Ri+CD40+αTNF-α/IFN-γ	0.010
CSF-1Ri+CD40+αIFN-γ	vs.	CSF-1Ri+CD40+αTNF-α/IFN-γ	0.010

Data are from one experiment (n = 3–6) representative of three independent experiments (total n = 6–15).

cell for an inflammatory response and T cell activation, which could serve as a potential molecular mechanism driving the emergence of polyfunctional inflammatory TAMs (Qiao et al., 2013; Kammertoens et al., 2017). Notably, TNF-α secretion by TAMs was robustly increased after CSF-1Ri+CD40 treatment, but IFN-γ was only weakly detected. In contrast, IFN-γ was markedly increased in T cells with CSF-1Ri+CD40 treatment, and depletion of T cells greatly decreased the effectiveness of CSF-1Ri+CD40 treatment. Thus, it is probable that a large portion of TNF-α is secreted by TAMs themselves, but that IFN-γ is primarily produced by T cells, and both of these secreted proteins cooperate to suppress tumor growth. These data suggest that a paracrine network between different immune cells might be necessary to coordinate a successful antitumor immune response. Further localization studies are required to understand the importance of localization and paracrine signaling within a tumor.

In summary, this study aids in identifying potential treatments that are tailored to microenvironments with poor

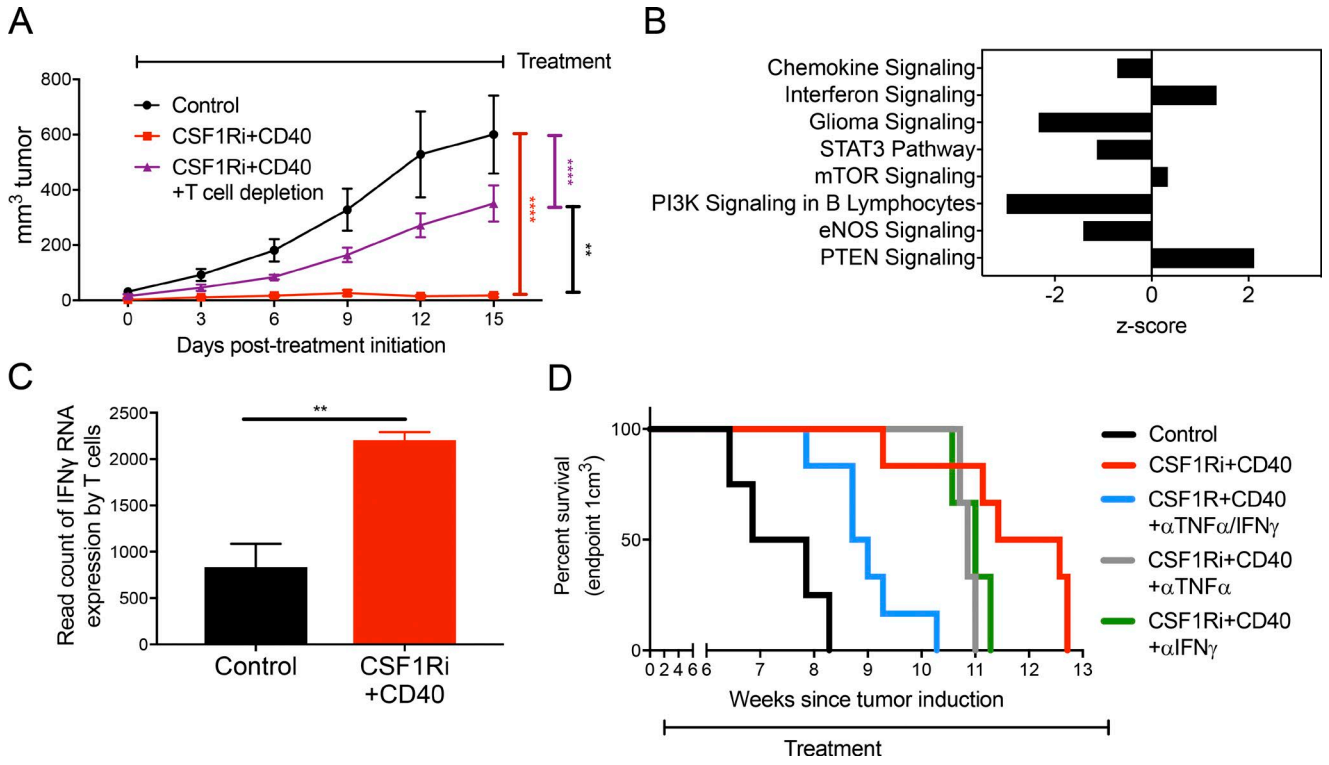

Figure 6. **Antitumor immunity provided by combined CSF-1Ri, and CD40 agonist therapy is partially dependent on T cells and on the inflammatory cytokines TNF-α and IFN-γ. (A)** T cell depletion interfered with tumor growth suppression from combined CSF-1Ri and CD40 agonist therapy. Braf/Pten mice were treated with CSF-1Ri (600 mg PLX6134/kg chow) and/or CD40 (10 mg FGK4.5/kg every 3 d), with or without T cell depletion (10 mg GK1.5 and TIB210/kg every 3 d), 30 d after tumor induction until end point (day 45) for a total of five treatments with FGK4.5 ± GK1.5/TIB210. Line graphs show the size of Braf/Pten melanomas over time. Data are presented as mean ± SEM of tumor size of two independent experiments (n = 6 for each group). Data were compared using one-way ANOVA with Holm-Sidak correction for multiple comparisons (day 45). **(B)** The top eight T cell pathways significantly modulated by CSF-1Ri+CD40 treatment compared with control identified by ingenuity pathway analysis (sorted by ascending p-values). Pathway analysis was performed on genes that had an absolute $\log_2$fold change >1 and $P < 0.05$. **(C)** *Ifng* transcription by $CD3^+$ T cells from control and CSF-1Ri+CD40-treated tumors. For B and C, cells were isolated from end point (day 60), and sorted in parallel with the TAMs in Fig. 4 A with the sort layout outlined in Fig. S1 A. Sorted cells were $CD3^+/CD45^+/CD11b^-$/LiveDEAD$^-$. Data are from two to three independent experiments (n = 2–3 each group, with three individual tumors pooled for each sample). **(D)** Kaplan-Meier curves show time to tumor end point (1 cm^3) in groups of Braf/Pten mice that were treated with CSF-1Ri chow (600 mg PLX6134/kg chow) and CD40 agonistic antibody (10 mg FGK4.5 clone/kg every 3 d i.p.) with or without TNF-α (10 mg XT3.11/kg every 3 d) and/or IFN-γ (10 mg XMG1.2/kg every 3 d) blocking antibody starting at day 30 after tumor induction. End point was tumor volume >1 cm^3. Data are from one experiment (n = 3–6) representative of three independent experiments (total n = 6–15). **, $P < 0.01$; ****, $P < 0.001$.

T cell infiltration and high TAM infiltration, which may offer hope for patients who fail to qualify for, have developed resistance to, or do not respond to PD-1– or CTLA-4–based regiments. Further studies on how CSF-1Ri+CD40 treatments might interact with checkpoint inhibitors are required, as a combination with T cell targeting treatments may be necessary to develop T cell memory and long-term durability.

MATERIALS AND METHODS

Mouse breeding and tumor induction

Braf^{CA}*; Tyr::CreER; Pten*$^{lox4-5}$ mice have been previously described (Dankort et al., 2009). Local tumor induction was performed as previously described (Ho et al., 2014). Age-matched mice that were housed in the same room of the same facility were used for each experiment. Mice were randomized to mouse size and litter, and treated mice were cohoused with controls whenever possible. The investigators were not blinded to mouse allocation. Group size was chosen based on constraints of age-matched litters. Tumors were measured by caliper. All mice were housed in the Yale Animal Resources Center in specific pathogen-free conditions. All animal experiments were performed according to the approved protocols of the Yale University Institutional Animal Care and Use Committee.

Tumor digestion

Tumors for flow cytometry and RNA sequencing were minced in HBSS with 0.5 mg/ml collagenase IV and 200 mg/L DNase, digested in a 37°C incubator for 30 min, and filtered to remove debris. Tumors for single cell barcode chip or intracellular cytokine stain were minced in complete RPMI with 5% serum, 0.5 mg/ml collagenase IV, and 200 mg/L DNase, digested in a 37°C incubator for 30 min, and filtered to remove debris. The filtrate was incubated with ammonium-chloride-potassium lysis buffer (Invitrogen) for 4 min, washed, and resuspended in complete RPMI. For RNA sequencing and single-cell secretion profiling, single-cell suspension was purified of dead cells with Lymphoprep (Stem Cell) per protocol. For RNA sequencing, at least three tumors were pooled for each sample collected in triplicate, with further characterization of phenotype by flow cytometry of each independent tumor.

Flow cytometry and cell sorting

Single-cell suspensions from tumors or splenocytes were incubated with anti-Fc receptor antibody (2.4G2) on ice for 15 min in complete RPMI with 10% serum. The cells were then stained with the appropriate antibodies in 2.4G2-containing 10% RPMI on ice for 30 min. For intracellular cytokine staining, cells were fixed in Fix/Perm (eBioscience) and stained with antibodies to detect intracellular cytokines, transcription factors, or other proteins (CSF-1Ri, CD206, Foxp3, TNF-α, and IFN-γ). Gating was performed with isotype controls of spleen and tumor samples; likewise, compensation was performed with spleen and tumor samples before being manually confirmed and compared with prior experiments. All samples were acquired on flow cytometers (LSR II; BD Biosciences) and analyzed with FlowJo (FlowJo, LLC). Cell sorting was performed on FACS Aria (BD Biosciences) in Yale Cell Sorter Core Facility. Cells for RNA sequencing were sorted into tubes containing RNAprotect (QIAGEN). TAMs were sorted based on the following markers: CD45$^+$/CD3$^-$/CD11b$^+$/Ly6G$^-$/LIVE/DEAD red$^-$. TANs were sorted based on the following markers: CD45$^+$/CD3$^-$/CD11b$^+$/Ly6G$^+$/LIVE/DEAD red$^-$. T cells were sorted based on the following markers: CD45$^+$/CD3$^+$/LIVE/DEAD red$^-$. The flow and sort gating is outlined in Fig. S1 A. Antibodies against CD45 (A20), CD8 (53-6.7), CD3 (145-2C11), CD4 (GK1.5), CD44 (IM7), CD11c (N418), CD11b (M1/70), Ly6C (HK1.4), Ly6G (1A8-Ly6G), Foxp3 (FJK-16s), and MHCII (M5/114.15.2) were purchased from eBioscience. Antibodies against CD4 (RM4-5), F4/80 (BM8), CD40L (MR1), PD-L1 (10F.9G2), CSF-1R (9-4D2-1E4), MHCI (KH95), CD80 (16-10A1), CD206 (C068C2), Ki-67 (16A8), TNF-α (MP6-XT22), IFN-γ (XMG1.2), and CD40 (3/23) were from Biolegend, and anti-CD86 (GL1) was from BD Biosciences. Antibody against CCR2 (475301) was from R&D Systems. LIVE/DEAD red was from Invitrogen.

In vivo treatments

30 d after tumor induction, when tumors were measurable but total volume less than 100 mm^3, *Braf*^{CA}*; Tyr::CreER; Pten*$^{lox4-5}$ mice received normal or CSF-1Ri PLX6134 chow (600 mg PLX6134/kg, provided by Plexxikon) for 30 d or until tumors reached end point (1 or 2 cm^3 as prespecified in each experiment). In various experiments, mice also received either control vehicle (PBS or isotype control), CD40 agonistic antibody (FGK4.5 10 mg/kg every 3 d i.p.), anti–TNF-α (XT3.11 10 mg/kg every 3 d), anti–IFN-γ (XMG1.2 10 mg/kg every 3 d), anti-CD4 (GK1.5 10 mg/kg every day), and anti-CD8 (TIB210 10 mg/kg every 3 d) for a total of 10 treatments or until prespecified tumor end point, or anti-Ly6G (1A8 25 mg/kg every 2 d) i.p., for a total of 14 treatments or until prespecified tumor end point.

Histological analysis

Tumors were fixed in 10% formalin and embedded in paraffin. Cut sections were prepared for histological analyses by performing H&E or IHC using F4/80 (6640 CI:A3 -1; Abcam) or CD3 (MC1477, CD3–12; AbD Serotec). Representative 40× fields were taken of the tumor samples using a BX41 microscope (Olympus) with an Insight 2 camera running SPOT Advanced 5.3 (SPOT Imaging). F4/80$^+$ and CD3$^+$ (brown) nuclei were counted per high-powered field (hpf; 400× = hpf) from tumors from two independent experiments, 6–15 hpf/tumor (n = 12–30).

RNA sequencing library preparation and data analysis

Total RNA was purified with the use of QIAzol and RNeasy Mini kit (QIAGEN), in which an on-column DNase treat-

ment was included. Purified RNA was submitted to the Yale Center for Genomic Analysis where it was subjected to mRNA isolation and library preparation. Nonstrand-specific libraries were generated from 50 ng total RNA using the SMARTer Ultra Low Input RNA for Illumina Sequencing kit. Libraries were pooled, six samples per lane, and sequenced on a high-throughput sequencing system (75-bp paired-end reads; HiSeq 2500; Illumina), and aligned using STAR to the GRCm38 (mm10) reference genome. A count-based differential expression protocol was adapted for this analysis (Anders et al., 2013); mappable data were counted using HTSeq and imported into R for differential expression analysis using the DESeq2. To find differentially regulated sets of genes for signature generation, a 1.5-$\log_2$fold change difference between samples and a p-adjusted (Holm-Sidak) $\leq$0.01 were used. For Ingenuity Pathway Analysis (QIAGEN), cutoffs of 0.5- or 1-$\log_2$fold change and a p-value $\leq$0.05 or an adjusted p-value $\leq$0.1 (as specified in each experiment) were used to select genes for pathway analysis, and only pathways with nonzero z-scores and $P < 0.05$ were selected. Accession numbers are available at Genome Expression Omnibus (GSE108753 and GSE108528).

Microwell assay for single-cell secretion profiling

The single-cell secretion profiling experiments were performed as previously described (Lu et al., 2013; Xue et al., 2015), with some modifications for the analysis of primary mouse TAMs. In brief, the capture antibodies (Table 2) were flow patterned onto epoxysilane-coated glass slides (SuperChip; ThermoFisher). The polydimethylsiloxane nanowell arrays and antibody barcode glass slides were blocked using complete RPMI + 10% FBS. Sorted cells were resuspended in complete RPMI with 20% FBS and supplemented with 125 nM of live cell marker (Calcein AM; ThermoFisher) to facilitate automatic live cell detection. The cells were added to the device, covered with the antibody barcode slide, secured with screws, and allowed to incubate for 8 h. At the end of the incubation period, the device was imaged with an automated inverted microscope (Eclipse Ti; Nikon) to record well position and cell locations. The device was then disassembled to perform the sandwich immunoassay. The glass slide was incubated with a mixture of detection antibodies (Table 2) for 1 h, followed by an incubation with 20 µg/ml streptavidin-APC (eBioscience) for 30 min, rinsed with PBS and water, and finally scanned with a Genepix 4200A scanner (Molecular Devices).

Single-cell secretion profiling data processing

Device images were analyzed using a custom script in MATLAB (MathWorks) to automatically detect well location and number of cells per well, extract all signals from each well, and process the data. In brief, after automatic well and live cell detection, signal image registration, and manual curation, the software automatically extracted the intensity signal from each antibody for all the nanowells in the device. The signal across the chip for each individual antibody was normalized by subtracting a moving Gaussian curve fitted to the local zero-cell well intensity levels. A secretion threshold for each antibody was then set at the 99th percentile of all normalized zero-cell wells. Finally, the data were transformed using the inverse hyperbolic sine with a cofactor set at 0.8× secretion threshold. To further visualize the data, previously described MATLAB-based software was used to create t-SNE maps (viSNE; Amir et al., 2013). Cluster analysis was performed with PhenoGraph using a euclidean distance metric, a previously described graph-based method for identifying subpopulations in high-dimensional single-cell data (Levine et al., 2015). Extracted clusters were analyzed using custom software written in MATLAB.

Table 2. **List of capture and detection antibody pairs used for single-cell secretion profiling**

Antibody pair	Vendor	Catalog no.
TNF-α	eBioscience	88-7324-88
CCL17	R&D	DY529
IL-12p40	BD Biosciences	555165
IL-10	BD Biosciences	555252
MMP9	R&D	DY6718
IL-6	R&D	DY406
IGF-I	R&D	DY791
CCL2	R&D	DY479
CCL8	R&D	DY790
Chi3l3	R&D	DY2446
CCL3	R&D	DY450
CXCL1	R&D	DY453
IFN-γ	R&D	DY485
CCL22	R&D	DY439
CCK5	R&D	DY478

Statistics

Data were presented in means ± SD unless otherwise specified. Statistical analysis was performed by Student's *t* test or one-way ANOVA and the Holm-Sidak method of correction for pairwise multiple comparisons as specified in the figure legends. Normal and equal distribution of variances was assumed. Survival in mouse experiments is shown as Kaplan-Meier curves, and the significance was calculated by log-rank test. Values were considered significant at $P < 0.05$ and are indicated as *, $P < 0.05$; **, $P < 0.01$; ***; $P < 0.005$; and ****, $P < 0.001$. All analyses were performed using Prism version 7.0 software (GraphPad).

For single-cell distributions, statistics was performed using a bootstrapping procedure to calculate the confidence intervals associated with sampling error in single-cell data. To obtain confidence intervals through bootstrapping, the single-cell datasets for each condition were sampled 10,000 times with replacement, and the metric of interest was calculated for each resampled dataset (i.e., fraction of cells secreting or signal intensity). We then calculated a 95% confidence interval for these resampled datasets, and statistical significance was assigned to pairwise comparisons that had nonoverlapping confidence intervals.

Online supplemental material

Fig. S1 shows the gating strategy used in all analyses and histograms relating to Fig. 1. Fig. S2 shows t-SNE plots from individual experiments. Fig. S3 shows frequency of immune cell types. Fig. S4 shows details of TAM pathway analysis and target expression. Fig. S5 shows neutrophil depletion and validation, as well as T cell depletion validation and *tnf* transcription.

ACKNOWLEDGMENTS

The authors thank Harriet Kluger for her insightful comments and discussion and all members of the Kaech, Bosenberg, and Miller-Jensen laboratories for insightful discussions and experimental advice.

This work was supported by the Yale School of Medicine Medical Scientist Training Program grant NIH/NIGMS T32 GM007205 to C.J. Perry and Yale Specialized Programs of Research Excellence in Skin Cancer (grant 5 P50 CA121974 to M. Bosenberg), a Wade F.B. Thompson/Cancer Research Institute–Clinic and Laboratory Integration Progarm grant, Oliver R. Grace and Wade F.B. Thompson Cancer Research Institute-CLIP grants to S.M. Kaech, a Melanoma Research Alliance grant (to S.M. Kaech and M. Bosenberg), the Melanoma Research Foundation (to M. Bosenberg), Yale Cancer Center Co-Pilot grant (to S.M. Kaech and K. Miller-Jensen), and National Institutes of Health grant 1 R01 GM123011-01 (to K. Miller-Jensen).

The authors declare competing financial interests: S.M. Kaech has sponsored research agreements with Roche and Med Immune. The authors have no further conflicts of interest to declare.

Author contributions: Conception: C.J. Perry, A.R. Muñoz-Rojas, K.M. Meeth, M. Bosenberg, K. Miller-Jensen, and S.M. Kaech. Development of methodology: C.J. Perry, A.R. Muñoz-Rojas, K.M. Meeth, R.A. Amezquita, M. Bosenberg, K. Miller-Jensen, and S.M. Kaech. Acquisition of data (provided animals, acquired and managed patients, provided facilities, etc.): C.J. Perry, A.R. Muñoz-Rojas, K.M. Meeth, L.N. Kellman, V.Y. Du, J.X. Wang, W. Damsky, L.N. Kellman, and A.L. Kuhlmann. Analysis and interpretation of data (e.g., statistical analysis, biostatistics, and computational analysis): C.J. Perry, A.R. Muñoz-Rojas, K. Miller-Jensen, S.M. Kaech, R.A. Amezquita, D. Thakral, and J.W. Sher. Writing, review, and/or revision of the manuscript: C.J. Perry, A.R. Muñoz-Rojas, K. Miller-Jensen, and S.M. Kaech. Administrative, technical, or material support (i.e., reporting or organizing data and constructing databases): R.A. Amezquita and D. Thakral. Study supervision: K. Miller-Jensen and S.M. Kaech.

Submitted: 9 August 2017
Revised: 20 November 2017
Accepted: 2 January 2018

REFERENCES

Amir, A.D., K.L. Davis, M.D. Tadmor, E.F. Simonds, J.H. Levine, S.C. Bendall, D.K. Shenfeld, S. Krishnaswamy, G.P. Nolan, and D. Pe'er. 2013. viSNE enables visualization of high dimensional single-cell data and reveals phenotypic heterogeneity of leukemia. *Nat. Biotechnol.* 31:545–552. https://doi.org/10.1038/nbt.2594

Anders, S., D.J. McCarthy, Y. Chen, M. Okoniewski, G.K. Smyth, W. Huber, and M.D. Robinson. 2013. Count-based differential expression analysis of RNA sequencing data using R and Bioconductor. *Nat. Protoc.* 8:1765–1786. https://doi.org/10.1038/nprot.2013.099

Beatty, G.L., E.G. Chiorean, M.P. Fishman, B. Saboury, U.R. Teitelbaum, W. Sun, R.D. Huhn, W. Song, D. Li, L.L. Sharp, et al. 2011. CD40 agonists alter tumor stroma and show efficacy against pancreatic carcinoma in mice and humans. *Science.* 331:1612–1616. https://doi.org/10.1126/science.1198443

Bhadra, R., J.P. Gigley, and I.A. Khan. 2011. Cutting edge: CD40-CD40 ligand pathway plays a critical CD8-intrinsic and -extrinsic role during rescue of exhausted CD8 T cells. *J. Immunol.* 187:4421–4425. https://doi.org/10.4049/jimmunol.1102319

Cassier, P.A., H. Gelderblom, S. Stacchiotti, D. Thomas, R.G. Maki, J.R. Kroep, W.T. van der Graaf, A. Italiano, B. Seddon, J. Dômont, et al. 2012. Efficacy of imatinib mesylate for the treatment of locally advanced and/or metastatic tenosynovial giant cell tumor/pigmented villonodular synovitis. *Cancer.* 118:1649–1655. https://doi.org/10.1002/cncr.26409

Dankort, D., D.P. Curley, R.A. Cartlidge, B. Nelson, A.N. Karnezis, W.E.J. Damsky Jr., M.J. You, R.A. DePinho, M. McMahon, and M. Bosenberg. 2009. Braf(V600E) cooperates with Pten loss to induce metastatic melanoma. *Nat. Genet.* 41:544–552. https://doi.org/10.1038/ng.356

Deryugina, E.I., E. Zajac, A. Juncker-Jensen, T.A. Kupriyanova, L. Welter, and J.P. Quigley. 2014. Tissue-infiltrating neutrophils constitute the major in vivo source of angiogenesis-inducing MMP-9 in the tumor microenvironment. *Neoplasia.* 16:771–788. https://doi.org/10.1016/j.neo.2014.08.013

Díaz-Valdés, N., M. Basagoiti, J. Dotor, F. Aranda, I. Monreal, J.I. Riezu-Boj, F. Borrás-Cuesta, P. Sarobe, and E. Feijoó. 2011. Induction of monocyte chemoattractant protein-1 and interleukin-10 by TGFbeta1 in melanoma enhances tumor infiltration and immunosuppression. *Cancer Res.* 71:812–821. https://doi.org/10.1158/0008-5472.CAN-10-2698

Flaherty, K.T., J.R. Infante, A. Daud, R. Gonzalez, R.F. Kefford, J. Sosman, O. Hamid, L. Schuchter, J. Cebon, N. Ibrahim, et al. 2012. Combined BRAF and MEK inhibition in melanoma with BRAF V600 mutations. *N. Engl. J. Med.* 367:1694–1703. https://doi.org/10.1056/NEJMoa1210093

Flaherty, K.T., S.J. Lee, F. Zhao, L.M. Schuchter, L. Flaherty, R. Kefford, M.B. Atkins, P. Leming, and J.M. Kirkwood. 2013. Phase III trial of carboplatin and paclitaxel with or without sorafenib in metastatic melanoma. *J. Clin. Oncol.* 31:373–379. https://doi.org/10.1200/JCO.2012.42.1529

Hauschild, A., J.-J. Grob, L.V. Demidov, T. Jouary, R. Gutzmer, M. Millward, P. Rutkowski, C.U. Blank, W.H. Miller Jr., E. Kaempgen, et al. 2012. Dabrafenib in BRAF-mutated metastatic melanoma: a multicentre, open-label, phase 3 randomised controlled trial. *Lancet.* 380:358–365. https://doi.org/10.1016/S0140-6736(12)60868-X

Ho, P.-C., K.M. Meeth, Y.-C. Tsui, B. Srivastava, M.W. Bosenberg, and S.M. Kaech. 2014. Immune-based antitumor effects of BRAF inhibitors rely on signaling by CD40L and IFNγ. *Cancer Res.* 74:3205–3217. https://doi.org/10.1158/0008-5472.CAN-13-3461

Hoves, S., C.-H. Ooi, C. Wolter, H. Sade, S. Bissinger, M. Schmittnaegel, O. Ast, A.M. Giusti, K. Wartha, V. Runza, et al. 2018. Rapid activation of tumor-associated macrophages boosts preexisting tumor immunity. *J. Exp. Med.* https://doi.org/10.1084/jem.20171440

Hussein, M.R. 2006. Tumour-associated macrophages and melanoma tumourigenesis: integrating the complexity. *Int. J. Exp. Pathol.* 87:163–176. https://doi.org/10.1111/j.1365-2613.2006.00478.x

Joyce, J.A., and J.W. Pollard. 2009. Microenvironmental regulation of metastasis. *Nat. Rev. Cancer.* 9:239–252. https://doi.org/10.1038/nrc2618

Kammertoens, T., C. Friese, A. Arina, C. Idel, D. Briesemeister, M. Rothe, A. Ivanov, A. Szymborska, G. Patone, S. Kunz, et al. 2017. Tumour ischaemia by interferon-γ resembles physiological blood vessel regression. *Nature.* 545:98–102. https://doi.org/10.1038/nature22311

Kaneda, M.M., K.S. Messer, N. Ralainirina, H. Li, C.J. Leem, S. Gorjestani, G. Woo, A.V. Nguyen, C.C. Figueiredo, P. Foubert, et al. 2016. PI3Kγ is a molecular switch that controls immune suppression. *Nature.* 539:437–442. https://doi.org/10.1038/nature19834

Kryczek, I., L. Zou, P. Rodriguez, G. Zhu, S. Wei, P. Mottram, M. Brumlik, P. Cheng, T. Curiel, L. Myers, et al. 2006. B7-H4 expression identifies a novel suppressive macrophage population in human ovarian carcinoma. *J. Exp. Med.* 203:871–881. https://doi.org/10.1084/jem.20050930

Larkin, J., V. Chiarion-Sileni, R. Gonzalez, J.J. Grob, C.L. Cowey, C.D. Lao, D. Schadendorf, R. Dummer, M. Smylie, P. Rutkowski, et al. 2015. Combined Nivolumab and Ipilimumab or Monotherapy in Untreated Melanoma. *N. Engl. J. Med.* 373:23–34. https://doi.org/10.1056/NEJMoa1504030

Levine, J.H., E.F. Simonds, S.C. Bendall, K.L. Davis, A.D. Amir, M.D. Tadmor, O. Litvin, H.G. Fienberg, A. Jager, E.R. Zunder, et al. 2015. Data-Driven Phenotypic Dissection of AML Reveals Progenitor-like Cells that Correlate with Prognosis. *Cell.* 162:184–197. https://doi.org/10.1016/j.cell.2015.05.047

Li, F., and J.V. Ravetch. 2011. Inhibitory Fcγ receptor engagement drives adjuvant and anti-tumor activities of agonistic CD40 antibodies. *Science.* 333:1030–1034. https://doi.org/10.1126/science.1206954

Lu, Y., J.J. Chen, L. Mu, Q. Xue, Y. Wu, P.H. Wu, J. Li, A.O. Vortmeyer, K. Miller-Jensen, D. Wirtz, and R. Fan. 2013. High-throughput secretomic analysis of single cells to assess functional cellular heterogeneity. *Anal. Chem.* 85:2548–2556. https://doi.org/10.1021/ac400082e

Maltby, S., N.G. Hansbro, H.L. Tay, J. Stewart, M. Plank, B. Donges, H.F. Rosenberg, and P.S. Foster. 2014. Production and differentiation of myeloid cells driven by proinflammatory cytokines in response to acute pneumovirus infection in mice. *J. Immunol.* 193:4072–4082. https://doi.org/10.4049/jimmunol.1400669

Mitchem, J.B., D.J. Brennan, B.L. Knolhoff, B.A. Belt, Y. Zhu, D.E. Sanford, L. Belaygorod, D. Carpenter, L. Collins, D. Piwnica-Worms, et al. 2013. Targeting tumor-infiltrating macrophages decreases tumor-initiating cells, relieves immunosuppression, and improves chemotherapeutic responses. *Cancer Res.* 73:1128–1141. https://doi.org/10.1158/0008-5472.CAN-12-2731

Ngiow, S.F., K.M. Meeth, K. Stannard, D.S. Barkauskas, G. Bollag, M. Bosenberg, and M.J. Smyth. 2016. Co-inhibition of colony stimulating factor-1 receptor and BRAF oncogene in mouse models of BRAFV600E melanoma. *OncoImmunology.* 5:e1089381. https://doi.org/10.1080/2162402X.2015.1089381

Piccolo, V., A. Curina, M. Genua, S. Ghisletti, M. Simonatto, A. Sabò, B. Amati, R. Ostuni, and G. Natoli. 2017. Opposing macrophage polarization programs show extensive epigenomic and transcriptional cross-talk. *Nat. Immunol.* 18:530–540. https://doi.org/10.1038/ni.3710

Pollard, J.W. 2004. Tumour-educated macrophages promote tumour progression and metastasis. *Nat. Rev. Cancer.* 4:71–78. https://doi.org/10.1038/nrc1256

Pyonteck, S.M., L. Akkari, A.J. Schuhmacher, R.L. Bowman, L. Sevenich, D.F. Quail, O.C. Olson, M.L. Quick, J.T. Huse, V. Teijeiro, et al. 2013. CSF-1R inhibition alters macrophage polarization and blocks glioma progression. *Nat. Med.* 19:1264–1272. https://doi.org/10.1038/nm.3337

Qian, B.-Z., and J.W. Pollard. 2010. Macrophage diversity enhances tumor progression and metastasis. *Cell.* 141:39–51. https://doi.org/10.1016/j.cell.2010.03.014

Qiao, Y., E.G. Giannopoulou, C.H. Chan, S.-H. Park, S. Gong, J. Chen, X. Hu, O. Elemento, and L.B. Ivashkiv. 2013. Synergistic activation of inflammatory cytokine genes by interferon-γ-induced chromatin remodeling and toll-like receptor signaling. *Immunity.* 39:454–469. https://doi.org/10.1016/j.immuni.2013.08.009

Ries, C.H., M.A. Cannarile, S. Hoves, J. Benz, K. Wartha, V. Runza, F. Rey-Giraud, L.P. Pradel, F. Feuerhake, I. Klaman, et al. 2014. Targeting tumor-associated macrophages with anti-CSF-1R antibody reveals a strategy for cancer therapy. *Cancer Cell.* 25:846–859. https://doi.org/10.1016/j.ccr.2014.05.016

Ryder, M., M. Gild, T.M. Hohl, E. Pamer, J. Knauf, R. Ghossein, J.A. Joyce, and J.A. Fagin. 2013. Genetic and pharmacological targeting of CSF-1/CSF-1R inhibits tumor-associated macrophages and impairs BRAF-induced thyroid cancer progression. *PLoS One.* 8:e54302. https://doi.org/10.1371/journal.pone.0054302

Tamoutounour, S., M. Guilliams, F. Montanana Sanchis, H. Liu, D. Terhorst, C. Malosse, E. Pollet, L. Ardouin, H. Luche, C. Sanchez, et al. 2013. Origins and functional specialization of macrophages and of conventional and monocyte-derived dendritic cells in mouse skin. *Immunity.* 39:925–938. https://doi.org/10.1016/j.immuni.2013.10.004

Tumeh, P.C., C.L. Harview, J.H. Yearley, I.P. Shintaku, E.J. Taylor, L. Robert, B. Chmielowski, M. Spasic, G. Henry, V. Ciobanu, et al. 2014. PD-1 blockade induces responses by inhibiting adaptive immune resistance. *Nature.* 515:568–571. https://doi.org/10.1038/nature13954

Ugel, S., F. De Sanctis, S. Mandruzzato, and V. Bronte. 2015. Tumor-induced myeloid deviation: when myeloid-derived suppressor cells meet tumor-associated macrophages. *J. Clin. Invest.* 125:3365–3376. https://doi.org/10.1172/JCI80006

Wang, J., C.J. Perry, K. Meeth, D. Thakral, W. Damsky, G. Micevic, S. Kaech, K. Blenman, and M. Bosenberg. 2017. UV-induced somatic mutations elicit a functional T cell response in the YUMMER1.7 mouse melanoma model. *Pigment Cell Melanoma Res.* 30:428–435. https://doi.org/10.1111/pcmr.12591

Wiehagen, K.R., N.M. Girgis, D.H. Yamada, A.A. Smith, S.R. Chan, I.S. Grewal, M. Quigley, and R.I. Verona. 2017. Combination of CD40 agonism and CSF-1R blockade reconditions tumor-associated macrophages and drives potent antitumor immunity. *Cancer Immunol. Res.* 5:1109–1121. https://doi.org/10.1158/2326-6066.CIR-17-0258

Winograd, R., K.T. Byrne, R.A. Evans, P.M. Odorizzi, A.R. Meyer, D.L. Bajor, C. Clendenin, B.Z. Stanger, E.E. Furth, E.J. Wherry, and R.H. Vonderheide. 2015. Induction of T-cell Immunity Overcomes Complete Resistance to PD-1 and CTLA-4 Blockade and Improves Survival in Pancreatic Carcinoma. *Cancer Immunol. Res.* 3:399–411. https://doi.org/10.1158/2326-6066.CIR-14-0215

Woo, S.-R., L. Corrales, and T.F. Gajewski. 2015. Innate immune recognition of cancer. *Annu. Rev. Immunol.* 33:445–474. https://doi.org/10.1146/annurev-immunol-032414-112043

Wynn, T.A., A. Chawla, and J.W. Pollard. 2013. Macrophage biology in development, homeostasis and disease. *Nature.* 496:445–455. https://doi.org/10.1038/nature12034

Xu, J., J. Escamilla, S. Mok, J. David, S. Priceman, B. West, G. Bollag, W. McBride, and L. Wu. 2013. CSF1R signaling blockade stanches tumor-infiltrating myeloid cells and improves the efficacy of radiotherapy in prostate cancer. *Cancer Res.* 73:2782–2794. https://doi.org/10.1158/0008-5472.CAN-12-3981

Xue, Q., Y. Lu, M.R. Eisele, E.S. Sulistijo, N. Khan, R. Fan, and K. Miller-Jensen. 2015. Analysis of single-cell cytokine secretion reveals a role for paracrine signaling in coordinating macrophage responses to TLR4 stimulation. *Sci. Signal.* 8:ra59. https://doi.org/10.1126/scisignal.aaa2155

Youn, J.-I., S. Nagaraj, M. Collazo, and D.I. Gabrilovich. 2008. Subsets of myeloid-derived suppressor cells in tumor-bearing mice. *J. Immunol.* 181:5791–5802. https://doi.org/10.4049/jimmunol.181.8.5791

Zhao, J., Z. Lv, F. Wang, J. Wei, Q. Zhang, S. Li, F. Yang, X. Zeng, X. Wu, and Z. Wu. 2013. Ym1, an eosinophilic chemotactic factor, participates in the brain inflammation induced by Angiostrongylus cantonensis in mice. *Parasitol. Res.* 112:2689–2695. https://doi.org/10.1007/s00436-013-3436-x